



This is a repository copy of *Enhanced Availability of Drivetrain Through Novel Multiphase Permanent-Magnet Machine Drive*.

White Rose Research Online URL for this paper:
<http://eprints.whiterose.ac.uk/97614/>

Version: Accepted Version

Article:

Patel, V.I., Wang, J. orcid.org/0000-0003-4870-3744, Nugraha, D.T. et al. (2 more authors) (2016) Enhanced Availability of Drivetrain Through Novel Multiphase Permanent-Magnet Machine Drive. *IEEE Transactions on Industrial Electronics*, 63 (1). pp. 469-480. ISSN 0278-0046

<https://doi.org/10.1109/TIE.2015.2435371>

Reuse

Unless indicated otherwise, fulltext items are protected by copyright with all rights reserved. The copyright exception in section 29 of the Copyright, Designs and Patents Act 1988 allows the making of a single copy solely for the purpose of non-commercial research or private study within the limits of fair dealing. The publisher or other rights-holder may allow further reproduction and re-use of this version - refer to the White Rose Research Online record for this item. Where records identify the publisher as the copyright holder, users can verify any specific terms of use on the publisher's website.

Takedown

If you consider content in White Rose Research Online to be in breach of UK law, please notify us by emailing eprints@whiterose.ac.uk including the URL of the record and the reason for the withdrawal request.



eprints@whiterose.ac.uk
<https://eprints.whiterose.ac.uk/>

Enhanced Availability of Drivetrain Through Novel Multi-Phase Permanent Magnet Machine Drive

Vipulkumar I. Patel, Member, IEEE, Jiabin Wang, Senior Member, IEEE, Dian T. Nugraha, Radovan Vuletić, and Jonas Touden

Abstract—This paper deals with novel multi-phase permanent magnet machine drive to enhance drivetrain availability in electric traction applications. It describes the development of new winding configurations for 6-phase permanent magnet (PM) brushless machines with 18-slot, 8-pole, that eliminate and/or reduce undesirable space harmonics in the stator magneto-motive force (MMF). In addition to improved power/torque density and efficiency with a reduction in eddy current loss in rotor permanent magnets and copper loss in end-windings, the developed winding configuration also enhances availability of drivetrain, in a variety of applications requiring a degree of fault tolerance, by employing it as two independent 3-phase windings in a 6-phase interior permanent magnet machine (IPM), which is designed and optimized for a given set of specifications for an electric vehicle (EV), under thermal, electrical and volumetric constraints. The paper also describes the design and development of 6-phase inverter with independent control for both sets of 3-phase windings. The designs of the motor and the inverter are validated by a series of preliminary tests on the prototype machine drive.

Index Terms—Electric vehicle, fractional-slot, inverter control, multiphase, permanent magnet machines, power drivetrain.

I. INTRODUCTION

PERMANENT MAGNET (PM) brushless machines have been increasingly used in a variety of applications ranging from high speed manufacturing [1], electric and hybrid vehicle traction [2], ship propulsion [3], aerospace actuation [4] to wind power generation [5]. To improve torque density and efficiency, and to reduce torque ripple, a relatively newer

winding configuration for PM brushless machines, which is often referred to as fractional-slot concentrated or modular, has recently emerged [2],[6],[7],[8]. It offers numerous advantages over the overlapped distributed winding in conventional PM brushless machines, which include simple manufacturing due to concentrated coils of the phase around one tooth or alternate teeth [9], higher copper packing factor and lower end-winding losses resulting into high efficiency [10], and reduced probability of inter-phase fault. Further, the modular winding arrangement gives rise to a high winding factor for the fundamental electro-motive force (EMF), while the effect on the 5th and 7th EMF harmonics is being significantly reduced. Such a modular or fractional-slot per pole per phase winding also yields extremely small cogging torque without the use of a skew [11] compared to conventional distributed windings in PM brushless machines.

In fractional-slot PM machines, however, the stator magneto-motive force (MMF) distribution contains a large number of space harmonics [2]. The lower and higher order space harmonics in the stator MMF rotate at different speeds relative to the rotor, and hence, cause many undesirable effects such as localized core saturation, eddy current loss in permanent magnets, acoustic noise and vibrations [12],[13]. These space harmonics also make it difficult to obtain high reluctance torque from interior permanent magnet (IPM) machines with fractional-slot windings [14].

A number of techniques, reported in the literature, to mitigate the above detrimental effects, include segmentation of magnets both axially and circumferentially [15], using different number of turns per coil side [16], and shifting of stator by mechanical angle to target specific MMF space harmonic [17]. All these techniques either increase the manufacturing cost and material wastage or impose challenges to achieve (a) higher torque density, (b) higher winding factor, and (c) ease of manufacturing. In order to eliminate the most harmful MMF space harmonics in a simple and cost-effective way, a novel fractional-slot per pole per phase winding configuration has been devised by Wang et al. [18], which improves both torque/power density and efficiency of various machine technologies for a variety of applications.

To improve safety and availability in electric traction applications, multiple 3-phase machine drives are advantageous [19],[20],[21]. Compared to conventional 3-phase machine drives, the multiple 3-phase machine drives are inherently fault tolerant [22],[23], as loss of one 3-phase

Manuscript received December 28, 2014; revised March 19, 2015 and April 13, 2015; accepted April 16, 2015.

Copyright (c) 2015 IEEE. Personal use of this material is permitted. However, permission to use this material for any other purposes must be obtained from the IEEE by sending a request to pubs-permissions@ieee.org.

This work was supported in part by the European Commission for CASTOR project under European Green Vehicles Initiative (EGVI) through Grant No. 260176.

V. I. Patel, and J. Wang are with the Department of Electronic and Electrical Engineering, The University of Sheffield, Sheffield, S1 3JD, United Kingdom (e-mail: v.i.patel@ieee.org, j.b.wang@sheffield.ac.uk).

D. T. Nugraha, and R. Vuletić are with the Automotive System Engineering Team, Infineon Technologies AG, Munich, 85579, Germany (e-mail: dian.nugraha@infineon.com, radovan.vuletic@infineon.com).

J. Touden is with the Hybrid Components Development Team, Volkswagen AG, Wolfsburg, 38436, Germany (e-mail: jonas.touden@volkswagen.de).

system will not lead to a complete loss of traction power. In addition, they have lower torque ripple, lower current per phase for the same voltage, lower DC link current harmonics, and improved torque-per-ampere capability [24].

Among quite a few research papers published in the area of multi-phase PM machine drives, only few focus on machine drive [20],[25] and most focus on various control algorithms [26],[27],[28] and fault-detection techniques [29],[30]. Villani et al. have described design and development of a 5-phase PM brushless DC motor drive for an aircraft flap actuator system in [20]. The majority of fault tolerant machine topologies described in the literature for EV applications are equipped with fractional-slot concentrated windings. However, these types of machines do not have significant reluctance torque [14]. Consequently, it is not possible to meet the two conflicting demands for high torque at low speeds and for low back-EMF at high speeds for safety without increasing inverter volt-ampere (VA) rating, which carries a significant cost penalty. Also, among all multi-phase PM machine drives reported in the literature, a full sized PM machine drive having merits of fractional-slot machines while exhibiting much higher reluctance torque for EV tractions has not been reported yet. Hence, this paper addresses this gap by design and development of 6-phase (2x3-phase) permanent magnet machine drive employing 18-slot, 8-pole, rated for 41kW peak power, for a segment-A electric vehicle, which is validated by a series of experiments on the prototype machine drive (motor and inverter), as part of industry-academia consortium on CASTOR project, which was funded by the European Commission. The project explored architectural advantages of fully integrated powertrain for EV propulsion system by proposing multi-phase machine with independent control to have lower footprint.

The novelty of this paper lies in various aspects of multi-phase machine drive for electric vehicles, such as: (a) novel fractional-slot winding configuration with high reluctance torque capability and reduced stator MMF space harmonics content, (b) drivetrain incorporating redundancy and safety with just one motor, leading to lower footprint, cost saving, and high reliability, (c) enhance availability in the event of open-circuit / short-circuit fault in one or two phases of a single 3-phase system, (d) adopting multiple 3-phase systems for fractional-slot-per-pole-per-phase winding configuration, and (e) a complete system design & prototyping for a representative electric vehicle, which is not presented in [18].

II. NOVEL MULTIPHASE PERMANENT MAGNET MACHINES FOR SEGMENT-A ELECTRIC VEHICLE

The authors have devised a novel fractional-slot-per-pole-per-phase winding configuration having topology of 18-slot 8-pole that can effectively reduce the most harmful space harmonics in a simple and cost-effective manner, and eliminate unbalanced magnetic forces associated with conventional 9-slot, 8-pole combination [18]. As discussed before, multiple three-phase motor drives are advantageous compared to conventional three-phase motor drives. Hence, to improve safety and to enhance drivetrain availability in traction applications, the authors have developed six-phase, 18-slot, 8-pole fractional-slot-per-pole-per-phase winding

configuration.

A. Novel 6-phase, 18-slot, 8-pole winding configuration

Fig. 1 shows the arrangement of 6-phase, 18-slot, 8-pole winding configuration. Each phase winding consists of three series-connected coils wired around two adjacent teeth with the polarity, as indicated by “+” and “-“. The stator windings, which are inserted in the stator slots, comprise six phases denoted as A, B, C, D, E, and F in Fig. 1. The coil span is two slot pitches, and the mechanical angle between two coil sides is $360^\circ/9 = 40^\circ$. The second three-phase windings (D-E-F) are positioned with respect to the first three-phase windings (A-B-C) by an offset of 180° mechanical or 9 slot pitches. The offset in electrical degrees is 720° or 4π . Thus, if phase windings A and D are arranged with the same polarity and similar arrangements are made for B and E, and C and F, respectively, the resultant fourth-order MMF space harmonic produced by the first three-phase windings (A-B-C) and the second three-phase windings (D-E-F) are in phase with respect to each other. The fourth-order space harmonic interacts with four-pole-pair rotor magnetic field to produce electromagnetic torque. For each odd ($n = 1, 3, 5, \dots$) space harmonic, the phase shift between the harmonic produced by the first three-phase winding and that by the second three-phase winding is $n\pi$. Thus, these harmonic have the same magnitude but in the opposite direction and hence will be canceled with each other by the proposed winding configuration.

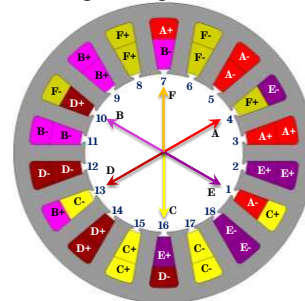


Fig. 1. Schematic of 6-phase, 18-slot, 8-pole winding configuration.

Thus, the winding configuration shown in Fig. 1 results in the highest possible winding factor of 0.945 for the fourth-order working space harmonic and completely eliminates all odd space harmonics. The end windings are slightly longer than in conventional tooth windings, whereas they are much shorter than in distributed windings. In addition, the end-windings of different phase coils, being in parallel, can be easily insulated using coil separators, which in turn reduce the likelihood of interphase faults. Furthermore, the normal magnetic force produced by the first three-phase windings is canceled by that produced by the second three-phase windings, thereby eliminating unbalanced magnetic pull in the radial direction, which leads to reduce bearing friction loss, noise, and vibration.

B. Drivetrain configuration, design specifications & design optimization

The above winding configuration is applied to the design of a traction machine for a segment-A sized electric vehicle with a centralized drivetrain configuration as shown in Fig. 2. As will be seen, the vehicle employs only one traction machine coupled to the front or the rear axle via a differential and a

TABLE I
DESIGN SPECIFICATIONS OF THE TRACTION MOTOR

Design specification	Symbol	Value
No. of phases	q	6
Base speed	ω_b	2800 r/min
Maximum cruise speed	ω_{ms}	11000 r/min
Maximum speed	ω_m	12000 r/min
Peak torque below and at base speed	T_{pk}	140 N·m
Rated torque below and at base speed	T_c	75 N·m
Maximum torque ripple w.r.t. peak torque	-	$\leq 5\%$
Peak power at base speed	P_{pk-b}	41 kW
Peak power at maximum cruise speed	P_{pk-ms}	32 kW
Continuous rated power	P_c	22 kW
Peak torque at maximum cruise speed	T_{ms}	27.8 N·m
Continuous torque at maximum cruise speed	T_{mc}	19.1 N·m
Nominal DC link voltage	V_{dc}	320 V
Maximum line-line voltage	E_m	650 V
Cooling medium & coolant inlet temperature	-	Water, 60°C
Permanent magnet material	-	Sm_2Co_{17}
Stator material, 0.35 mm thick lamination	-	M270-35A
Rotor material, 0.20 mm thick lamination	-	NO20

TABLE II
DESIGN CONSTRAINTS FOR THE TRACTION MOTOR

Design Parameter	Symbol	Constraints
Stator outer radius	RAD2	75 mm
Stack length of the motor	L_{stk}	≤ 150 mm
Continuous current density	J_c	≤ 10 A/mm ²
Maximum flux linkage	ψ_m	≤ 74.7 mWb
Maximum motor current - peak	I_m	≤ 200 A
d-axis inductance	L_d	$0.256 \leq L_d \leq 0.721$ mH
Copper winding temperature	T_{cu}	$\leq 180^\circ\text{C}$ (class H)
Steel lamination temperature	T_{fe}	$\leq 225^\circ\text{C}$
Permanent magnet temperature	T_{pm}	$\leq 200^\circ\text{C}$ (Recoma 28)

reduction gearbox. The six phases of the electric machine are controlled as two separate and independent three-phase systems, which are fed by two independent inverters. In the event of fault on one of the three-phase drive system, the vehicle can continue to operate using the remaining healthy set of three-phase drive system without any sudden stops or compromising vehicle stability and passenger safety. The ability of the proposed winding topology with 18-slot, 8-pole to configure it as two sets of three-phase systems enhances the availability of the centralized drivetrain.

From the vehicle data and acceleration performance requirements [31], the design specifications for the motor can be obtained [32], which are listed in Table I. In addition to design specifications, thermal, electrical, and volumetric constraints are given in Table II. The flux linkage due to permanent magnets ψ_m must be constrained to limit the voltage below the maximum permissible peak line-to-line voltage in the event of an inverter fault $V_{m-line-line} \leq E_m$. The maximum peak motor current I_m is limited by the inverter VA rating. The torque ripple must be below 5% for passenger comfort and ease of noise and vibration harness. In addition, the d-axis inductance must be kept within a maximum and a minimum value range [33] in order to satisfy the constant power profile given in Table I.

It is important to note, since an EV operates over a wide torque-speed range, a design optimized against the rated torque at the base speed does not necessarily lead to an optimal design over a given driving cycle [34]. Hence, the objective of the design optimization was to achieve the best torque production at the base speed while minimizing the

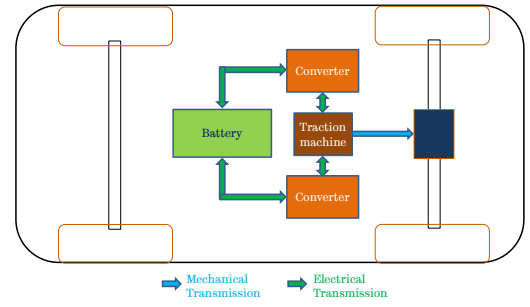


Fig. 2. Power drivetrain of a segment-A electric vehicle (EV).

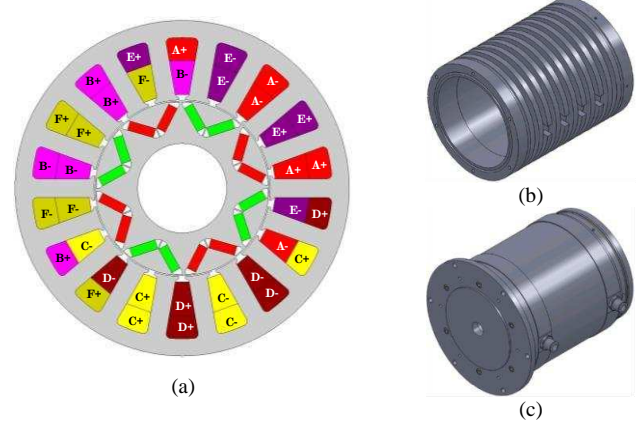


Fig. 3. (a) Optimized cross-section of 6-phase, 18-slot, 8-pole IPM machine. (b) Cooling chamber. (c) Motor enclosure comprising cooling chamber, sleeve and end plates.

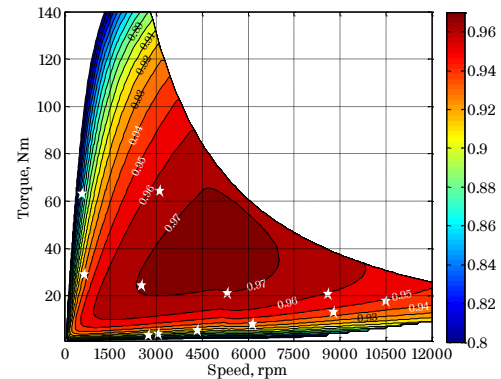


Fig. 4. Predicted efficiency map of 6-phase, 18-slot, 8-pole IPM machine.

TABLE III
PERFORMANCE OF THE OPTIMIZED MOTOR

	Unit	Rated torque at base speed	Peak torque at base speed	Max. cruise speed operation
Total Torque	N·m	75.0	140.0	19.1
% Reluctance torque	%	59.1% (using frozen permeability)		
Torque ripple	%	2.5	5.0	2.2
Speed	r/min	2800	2800	11000
Peak current	A	77.0	191.0	54.7
Voltage ($V_{line-line}$)	V	217.9	319.9	322.6
Current density	A/mm ²	10.1	25.1	7.2
Copper loss	W	942	5796	475
Iron loss	W	178	276	647
PM eddy current loss	W	18	116	86
Efficiency	%	95.1	86.9	94.8
NEDC energy efficiency	%	95.2		

losses over the representative driving cycle, i.e., new European driving cycle (NEDC). The leading design parameters of a typical single layer, V-shaped, interior

permanent magnet machine (IPM) are optimized against the objectives subject to the specifications and constraints through a combination of analytical and 2-D finite-element-analyses (FEA), including mechanical stress analysis for rotor and thermal design for the machine, as explained in [33]. Fig. 3 (a) shows the optimized cross-section of 6-phase, 18-slot, 8-pole IPM machine. It is worthwhile to note that the phase shift between two sets of three-phase systems (A-B-C and D-E-F) is 20° instead of usual 60° and is realized by 13 slot-shifts between A-B-C and D-E-F, which further helps in reducing MMF space harmonics while maximizing torque capability, as explained in [33]. This configuration is used for the design and prototyping. Fig. 3 (b) shows cooling chambers with grooves for coolant, whereas Fig. 3 (c) shows motor enclosure comprised of cooling chamber, sleeve and end plates. The cooling system design is explained in detail in [35].

C. Performance prediction

Table III shows the performance prediction of the optimized machine at the rated torque and the peak torque operations at the base speed as well as at the maximum cruise speed operation. The energy efficiency over the NEDC is calculated using energy center of gravity principle [36], for 12 discrete torque-speed points (shown as stars in Fig. 4), using (1).

$$\eta_{\text{NEDC}} = \frac{\sum_{i=1}^{12} \omega_i T_i dt_i}{\sum_{i=1}^{12} \omega_i T_i dt_i + \sum_{i=1}^{12} (P_{\text{cu}-i} + P_{\text{fe}-i}) dt_i} \quad (1)$$

where ω_i is the angular speed in rad/s, T_i is the torque in N·m, dt_i is the time duration, $P_{\text{cu}-i}$ and $P_{\text{fe}-i}$ are the copper loss and the iron loss for the i^{th} point, respectively.

The predicted efficiency map of the motor is shown in Fig. 4, which includes iron loss derived from 2-D FEA and copper loss using predicted resistance at 120°C . It is evident that the designed IPM motor exhibits high efficiency as well as high reluctance torque over wide torque-speed range of the traction vehicle. Also, the torque ripple of the designed machine with proposed winding configuration, over entire torque-speed range, is below the requirement of 5% for EV applications.

III. MULTI-PHASE INVERTER DESIGN

As part of the research project, multi-phase inverter design to control multi-phase permanent magnet machine was carried out. This section presents holistic approach of the multi-phase inverter design combining inputs from the study of the multi-phase machine characteristics and the requirements from the OEM partner.

A. Design requirements for the inverter

In terms of the torque-speed envelope, the design specifications for the multi-phase inverter remains same as that of multi-phase permanent magnet machine. In addition, the requirement is to have independent control for both three-phase systems of the multi-phase PM machine, as shown in Fig. 2. Hence, two independent inverters sharing the same DC bus link are required. The inverter should be water-cooled to integrate the cooling circuit of the machine and the inverter together in a segment-A electric car.

From motor design point of view, the influence of voltage rating on the motor size and performance can be virtually eliminated by fine-tuning. However, if the voltage is too low, the current rating will be high and the cable and winding wire size increases, which will increase the cable mass, cable loss and losses in the connection leads as well as contactors. Further, a thicker winding wire will increase difficulties in winding insertion process and reduce slot filling factor, etc., which is not desirable for high efficiency. On the other hand, a low voltage rating makes insulation less demanding and is conducive to better reliability. In contrast the voltage rating has a much greater influence on the inverter efficiency and cost as well as on the complexity and reliability of battery packs. As the power rating of the drivetrain under consideration is relatively high, a high voltage would be advantageous for reducing cable size and parasitic losses in the connection leads and control switches. Given that 650V IGBT devices are mass-produced and very cost-effective, 320V nominal DC link voltage may be appropriate for design.

B. Hardware design

1) Selection of power modules

Among various power modules available in the industry, Table IV lists the power modules considered for the design under consideration. The HybridPACKTM1 was chosen with two different dies with 650V IGBT3 and 1200V IGBT4. The Easy2BTM was also considered with 400V and 1200V. Fig. 5 shows the digital imprint of these two power modules, whereas Table IV lists the ratings of these power modules.

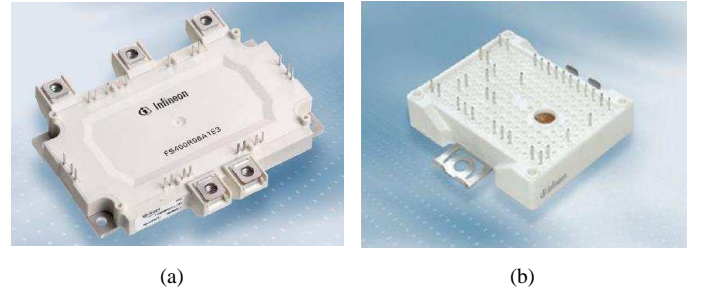


Fig. 5. Various power modules for the design of multi-phase inverter. (a) HybridPACKTM1 power module. (b) EasyPACKTM2B power module.

TABLE IV
VARIOUS POWER MODULES FOR THE DESIGN

	Current (A)	Voltage (V)	Cooling
HybridPACK TM 1	200	650	Water
	400	650	Water
	200	1200	Water
EasyPACK TM 2B	400	400	Water
	200	1200	Water

The selection of power modules for the design of multi-phase inverter was made based on efficiency and cost attributes. The design simulations were carried out to meet output power requirement of 40kW at the peak torque of 140 N·m and at the base speed of 2800 r/min with water inlet temperature of 70°C and maximum chip temperature of 150°C . If the chip temperature exceeds 150°C , then simulated design is discarded. Fig. 6 shows the efficiency of HybridPACKTM1 and EasyPACKTM2B power modules under consideration. The efficiency calculation is carried out using IGBT manufacturer calculation tool IPOSIM, one example of using it is given in

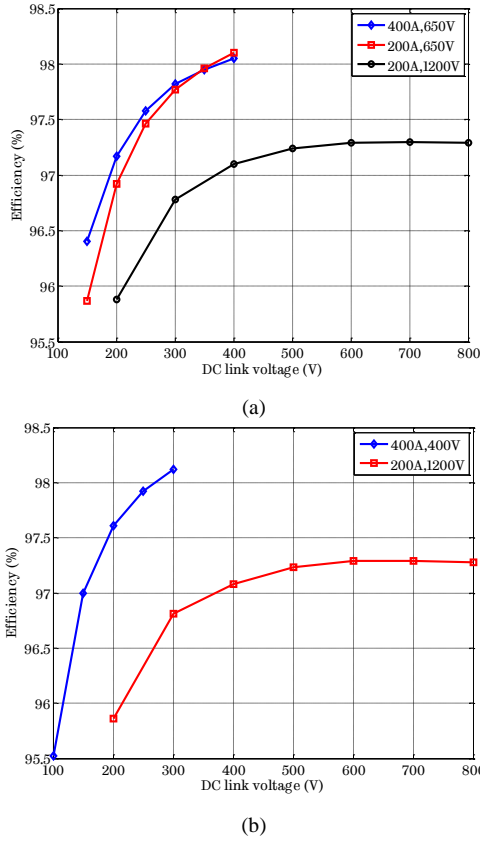


Fig. 6. Predicted efficiency of power modules under consideration. (a) HybridPACK™1 power modules. (b) EasyPACK™2B power modules.

[37]. As seen, HybridPACK™1 exhibits higher efficiency at 320V DC link voltage compared to EasyPACK™2B 1200V power modules. Also, 650V modules are more efficient than 1200V modules for the application under consideration.

As the efficiency of both 200A/650V and 400A/650V HybridPACK™1 differs only little ($\pm 0.05\%$) over DC link voltage range of 300V to 400V, the selection now depends on the cost of power modules. HybridPACK™1 with 200A will require only 6 chips per inverter compared to 12 chips of 400A module. Hence, two HybridPACK™1 with 200A/650V ratings are selected for the design of multi-phase inverter.

2) Inverter topology

With respect to voltage level, efficiency and cost, the simulation with HybridPACK™1 200A/650V IGBT modules delivered the best. In order to achieve peak power of 40kW at the base speed of 2800 r/min for the power drivetrain, two HybridPACK™1 200A/650V modules are used in 2x3-phase inverter topology. Each module is specifically designed for HEV applications with a maximum supply voltage of 450V and a power range up to 20kW. Designed for a junction operation temperature at 175°C, the module accommodates a six-pack configuration of 3rd generation Trench-Field-Stop IGBTs and matching emitter controlled diodes, which are rated up to 400A/650V. It is based on IGBT Technology, which offers lowest conduction and switching losses.

IGBT modules can be directly mounted on to a water cooled heat sink directly to form a compact inverter. The driver board PCB is soldered on top of the power module to make the whole drive compact and efficient. All power

connections to the motor cables are realized with screw terminals. A complete 6-phase inverter, which consists of two HybridPACK™1 power module, two DC link capacitors, two driver boards, one adopter board and a heat sink beneath the power modules is shown in prototype section.

C. Control system design

6-phase motor can operate as a single unit, in which the stator windings are excited with 6-phase balanced sinusoidal currents of the same magnitude and frequency but having a phase shift of 60° electrical with respect to each other. However, 6-phase motor can also be controlled as two separate and independent three-phase systems. Each set of the three-phase system is excited with 3-phase balanced sinusoidal currents of the same magnitude and frequency but having a phase shift of 120° electrical with respect to each other. The two sets of three-phase systems are excited with phase shift of 20° electrical with each other. The magnitude of the current in the two three-phase systems are controlled independently. In particular, if one three-phase system is failed due to either an open-circuit or short-circuit fault, the remaining healthy three-phase system is able to provide about 50% torque and power output. The control system design is based on this objective to achieve enhanced availability for the power drivetrain under consideration.

1) d-q axis model of the multi-phase IPM machine

The d-q axis model of the machine is given by:

$$L_d \frac{di_d}{dt} + Ri_d = v_d + \omega L_q i_q \quad (2)$$

$$L_q \frac{di_q}{dt} + Ri_q = v_q - \omega L_d i_d - K_e \omega_m \quad (3)$$

where V_d and V_q are d- and q-axis voltages, i_d and i_q are d- and q-axis currents. L_d and L_q are d- and q-axis inductances, respectively, ω and ω_m are electrical and mechanical angular speed, respectively, R is the phase resistance, $K_e = p\psi_m$ is the back EMF constant, p is pole-pair number, and ψ_m is the peak flux-linkage per phase due to permanent magnet field.

The electromagnetic torque expressed in d-q axis variables is given by (4).

$$T_e = \frac{qP}{2} [\psi_m i_q + (L_d - L_q) i_d i_q] \quad (4)$$

where q ($=6$) is the number of phases.

The general 6-phase to d-q axis transformation for the designed 6-phase IPM machine is given by (5).

$$C_{dq \leftarrow ABCDEF} = \frac{2}{q} \begin{bmatrix} \cos \theta & \cos(\theta - 120^\circ) & \cos(\theta + 120^\circ) \\ -\sin \theta & -\sin(\theta - 120^\circ) & -\sin(\theta - 120^\circ) \\ \dots & \dots & \dots \\ \cos(\theta - 20^\circ) & \cos(\theta - 140^\circ) & \cos(\theta + 100^\circ) \\ \dots & \dots & \dots \\ -\sin(\theta - 20^\circ) & -\sin(\theta - 140^\circ) & -\sin(\theta - 100^\circ) \end{bmatrix} \quad (5)$$

And, the inverse transformation is,

$$C_{ABCDEF \leftarrow dq} = \begin{bmatrix} \cos \theta & -\sin \theta \\ \cos(\theta - 120^\circ) & -\sin(\theta - 120^\circ) \\ \cos(\theta + 120^\circ) & -\sin(\theta + 120^\circ) \\ \cos(\theta - 20^\circ) & -\sin(\theta - 20^\circ) \\ \cos(\theta - 140^\circ) & -\sin(\theta - 140^\circ) \\ \cos(\theta + 100^\circ) & -\sin(\theta + 100^\circ) \end{bmatrix} \quad (6)$$

The mechanical equation for the system is given by (7).

$$J \frac{d\omega_m}{dt} = (T_e - T_L - B\omega_m) \quad (7)$$

where J is the moment of inertia of the system, and B is viscous friction coefficient, T_L is the load torque, T_e is electromagnetic torque of the motor whether it operates as 6-phase machine, or as two independent 3-phase machines.

2) Parameters of the multi-phase IPM machine

Because of interior mounted PM structure of the designed 6-phase, 18-slot, 8-pole machine, d- and q-axis inductances vary not only with motor currents but also with rotor position. In order to derive the inductance map of the machine, 2-D static FEA with rotor rotation is carried out over an electric cycle for a range of i_d and i_q currents. When the machine is modelled as two independent three-phase systems, the cross-coupling between the two systems is neglected as the mutual inductances between two 3-phase systems are just 4-5%. However, the variation of d- and q-axis inductances with d- and q-axis current, and cross-saturation effect on PM flux linkage due to q-axis current are taken into account. The inductance values are averaged over an electrical cycle. Fig. 7 (a) and (b) shows the variation in d- and q-axis inductances with d- and q-axis currents respectively. Fig. 8 shows the cross-saturation effect on PM flux linkage due to q-axis current. These inductance maps along with cross-saturation in PM flux linkage are incorporated as look-up tables in the inverter control system to control the motor in various modes, i.e. current control mode/torque control mode and speed control mode in constant torque and field weakening regions.

3) Control system

Since the mutual coupling between the two 3-phase sets is very small and can be neglected, the two 3-phase systems are controlled independently. This has the benefit that in an event of fault(s) in one 3-phase set, the other set does not need to reconfigure its controller. Alternatively, the two 3-phase sets may be controlled as a single unit by employing “vector-space decomposition” (VSD) algorithm [38]. While the VSD may be a better option for symmetrical nx3-phase machines, it requires control reconfiguration under fault conditions. Further, with two independent controls implemented in two d-q reference frames, the effect of high order back-EMF harmonics will be suppressed by the current feedback control loop.

Look-up tables to generate current references from torque reference are derived using inductance and flux-linkage maps

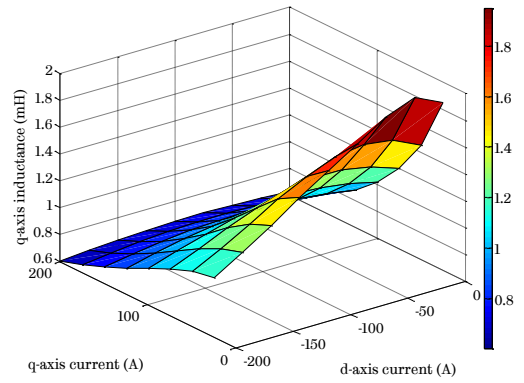


Fig. 7. Inductance map of 6-phase, 18-slot, 8-pole IPM machine. (a) d-axis inductance map. (b) q-axis inductance map.

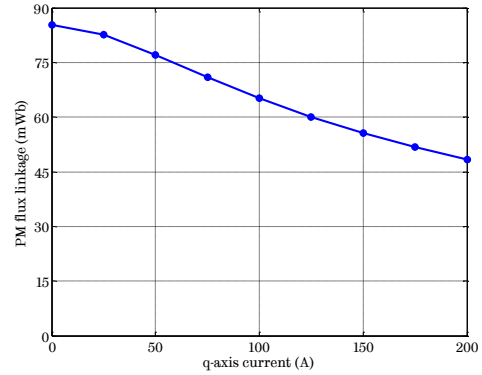


Fig. 8. Cross-saturation on PM flux linkage due to q-axis current.

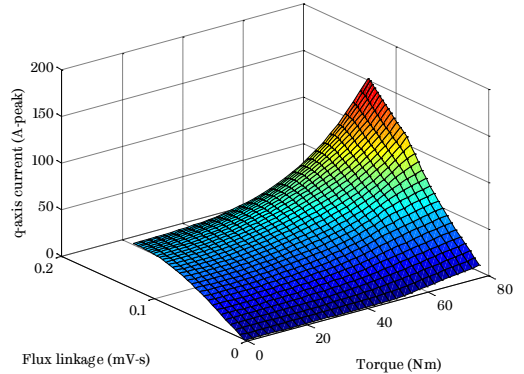
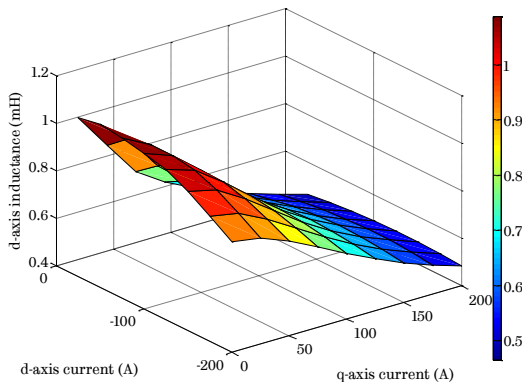


Fig. 9. Look-up table to generate q-axis reference from torque and flux reference.



(a)

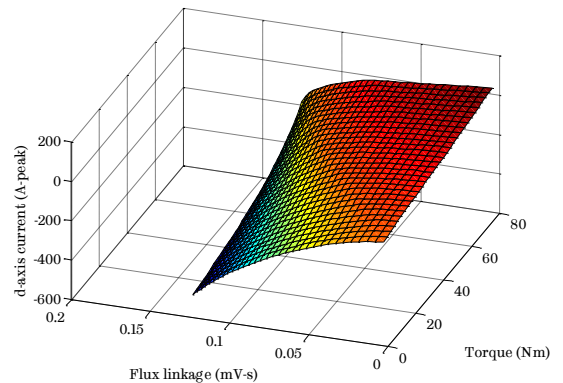


Fig. 10. Look-up table to generate d-axis reference from torque and flux reference.

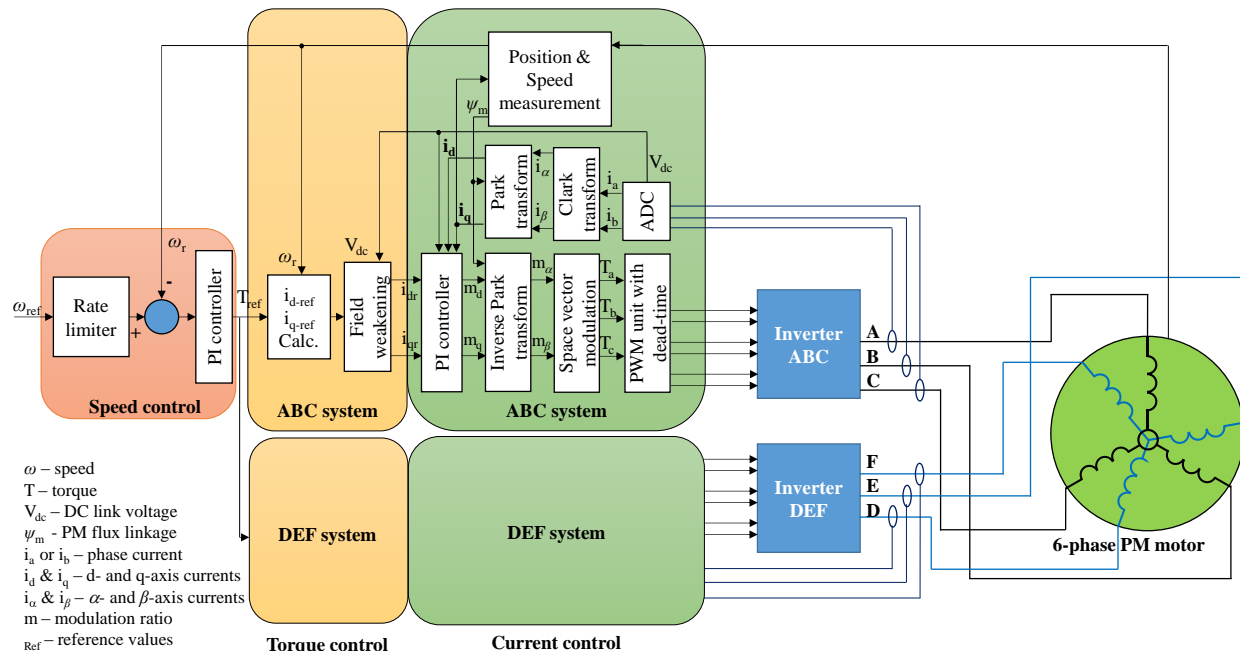


Fig. 11. Schematic of inverter control system having independent control for both set of three-phase system of 6-phase permanent magnet machine.

of each 3-phase set, which are shown in Fig. 9 and Fig. 10 respectively, and are embedded in the control system. Fig. 11 shows the schematic of control system developed for independent control of both sets of three-phase systems (ABC and DEF) of designed 6-phase PM machine, showing speed control, torque control and current control.

In speed control mode, the speed controller generates the torque reference from the reference speed set by the user input. It works in conjunction with both torque control and speed control loops to generate the required d- and q-axis currents for the desired speed. In torque control mode, the torque controller generates d- and q-axis current references from (a) the torque reference, and (b) rotor speed and DC-link voltage. The d- and q-axis current references are then tracked by the current controller. The voltages from the controller outputs are conditioned by an over-modulation block whose outputs are used by space vector modulator to generate pulse-width-modulation (PWM) pulses, which are fed to the inverter to generate the phase voltages applied to the motor terminals.

The controller works in maximum-torque-per-ampere (MTPA) when the line-to-line voltage of the machine is $<320V$, whereas it works in field-weakening or maximum-torque-per-voltage (MTPV) when the line-to-line voltage of the machine is limited to $320V$. The development and implementation of the control software is carried out using Matlab/Simulink with embedded code generator and dedicated compiler/debugger.

IV. PROTOTYPES AND EXPERIMENTAL VALIDATION

A prototype machine employing the novel 6-phase, 18-slot, 8-pole winding configuration and a prototype inverter having two independent controls for each three-phase system have been constructed to validate the designs for the given specifications in Table I.

A. Prototype details

Fig. 12 (a) shows the stator and the rotor laminations, stator frame with cooling chamber, and stator assembly, whereas the rotor assembly and motor assembly of the prototype motor are shown in Fig. 12 (b) and (c), respectively. The prototype 6-phase inverter with independent control for each three-phase system along with cooling water circuit, data communication, and dc power link is shown in Fig. 13.

The performance of the prototype drivetrain has been measured on the test rig at OEM's facilities, shown in Fig. 14,

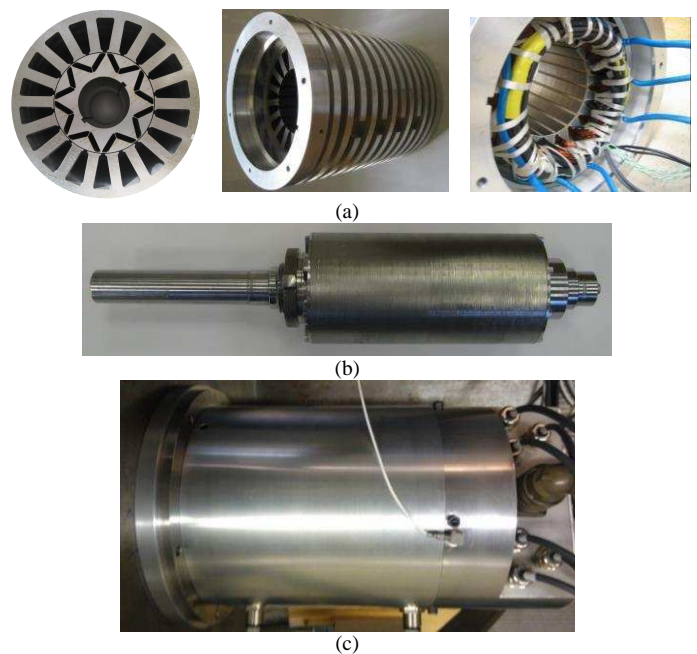


Fig. 12. Components of the prototype machine employing 6-phase, 18-slot, 8-pole winding configuration. (a) Laminations, stator frame, and stator assembly. (b) Rotor assembly. (c) Motor assembly.

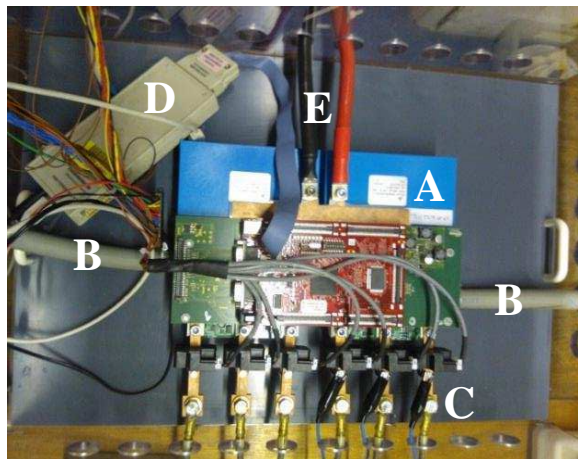


Fig. 13. Components of the prototype 6-phase inverter with independent controls for each three-phase systems. (A) Inverter with independent control. (B) Cooling water circuit. (C) Inverter output terminals. (D) Data communication. (E) DC power link.

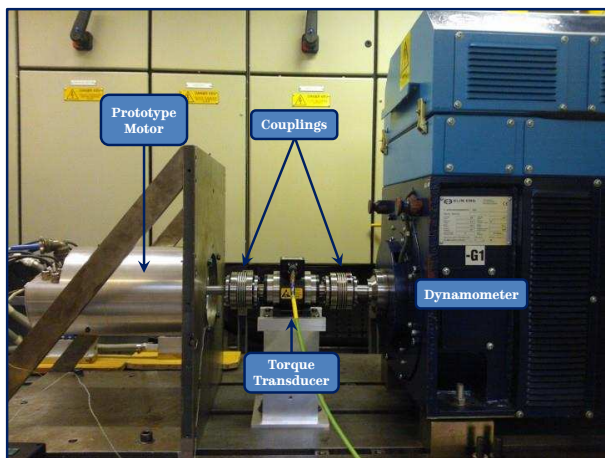


Fig. 14. Test bench to measure performance of the prototype power drivetrain.

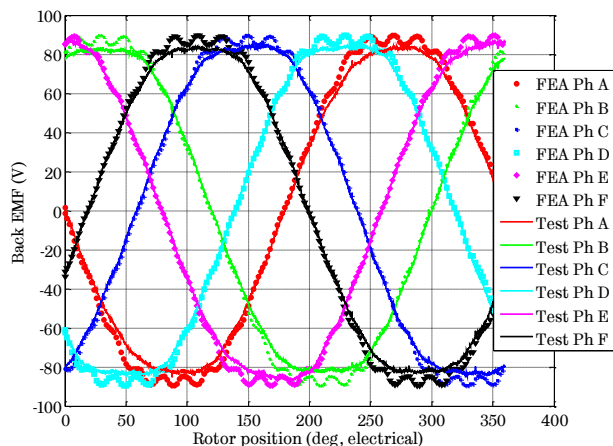


Fig. 15. Comparison of measured and predicted back EMFs of prototype 6-phase, 18-slot, 8-pole IPM machine at base speed of 2800 r/min.

in which, the prototype motor is coupled to the dynamometer using via an in-line torque transducer. The dynamometer, which is controlled by a bidirectional four-quadrant converter, is used to drive the motor at a given speed and provides load torque during the load test. The motor is controlled by a prototype six-phase inverter, shown in Fig. 13, configured as

two independent three-phase inverters that operates in torque control mode and can achieve flux-weakening operation in a high-speed range. The inverter dc-link power is fed by a programmable bidirectional dc power supply. The six-phase input power to the motor, which is also an output power of the inverter is measured by two 4-channel power analyzers, whereas the output power of the motor is measured by the in-line torque transducer. The power analyzer also measures the input power to six-phase inverter. Thus, the test rig shown in Fig. 14 allows direct and precise measurement of the motor and the inverter efficiency.

B. Back EMF and no-load iron loss

Fig. 15 compares the measured and the finite-element (FE) predicted back EMF waveforms of all six phases at the base speed of 2800 r/min. From the comparison, it is found that the RMS and the peak values of the measured phase back EMF are 7.7% and 6.8% lower than the prediction. The prediction is made using the measured properties of the magnet, supplied by the manufacturer, and at the same temperature at which the test is conducted. The difference can be attributed to lower permanent magnet width in the prototype due to grinding or tolerance requirement for inserting them inside the rotor, and the resulting air-gap between the magnets and rotor core, as well as slightly different BH characteristics of the laminations between the datasheet and the actual materials used in the prototype. 3-D effect and axial leakage flux at both ends of the rotor may also contribute to the low measured back EMF, since the FE predictions are performed in 2-D.

The no-load tests with the prototype rotor and a dummy rotor were carried out using an in-line torque transducer with a range of 0-20 N·m. The dummy rotor has the same mass and mechanical dimensions as the prototype rotor. The no-load iron loss is therefore obtained by subtracting the no-load loss with dummy rotor from that with the prototype rotor. Fig. 16 shows the comparison of predicted and measured no-load iron losses from standstill to maximum speed. It does not include mechanical losses. It can be seen that, by introducing a build factor of 1.24 that accounts for any deterioration of material properties of laminations, the calibrated no-load iron loss model matches very well with the measured no-load iron loss.

C. Efficiency map of 6-phase drivetrain

Fig. 17 (a), (b) and (c) show the measured efficiency map of the motor, the inverter, and the combined drivetrain respectively, with drive operation at 320V. Compared with the predicted efficiency map of the motor, as shown in Fig. 4, the measured efficiency is lower by 1-2%. Apart from measurement errors, the difference is attributable to a number of other factors. First, the efficiency reduction is contributed by the increase in the measured iron loss by 24% known as “build factor”, which accounts for the iron loss increase during the manufacturing process. The reduction of measured phase back-EMF also results in less PM torque, and hence lower efficiency. It should be noted that the bearing friction and windage loss are not included in the prediction but they also contribute to the reduction in efficiency. As seen, the efficiency of the designed drivetrain is high over wide torque-speed range of the traction application under consideration.

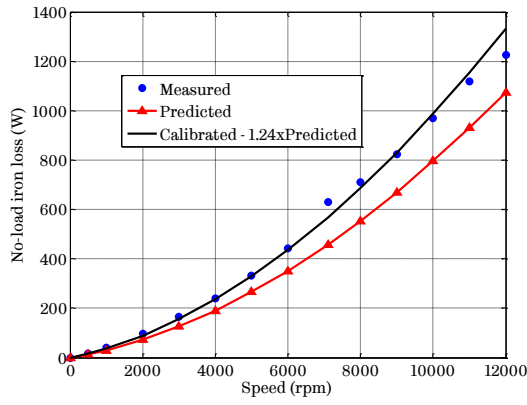


Fig. 16. Comparison of measured and predicted no-load iron loss of prototype 6-phase, 18-slot, 8-pole IPM machine.

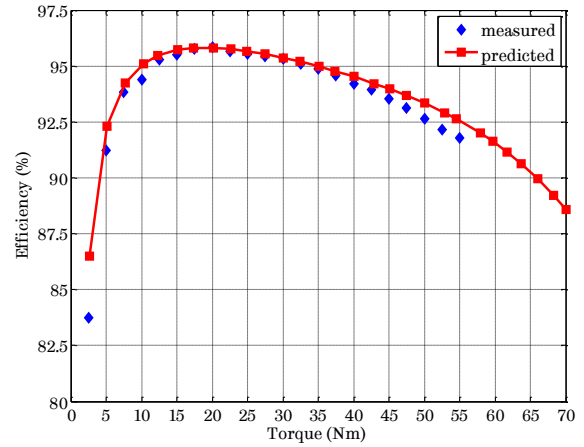
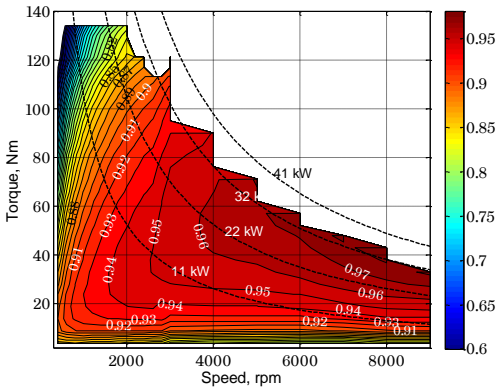
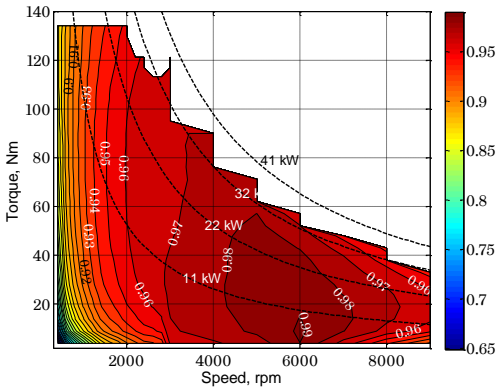


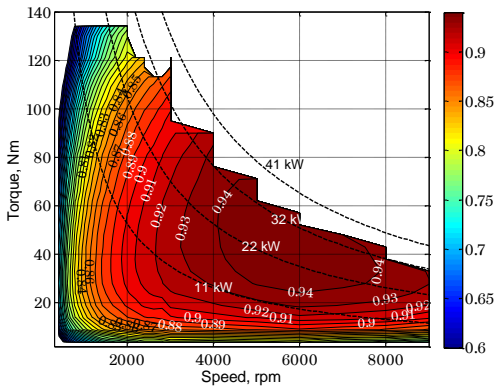
Fig. 18. Comparison of measured and predicted efficiency of 6-phase, 18-slot, 8-pole IPM prototype machine under 3-phase operation (A-B-C supplied by inverter, and D-E-F open circuited) at the base speed of 2800 r/min.



(a)



(b)



(c)

Fig. 17. Measured efficiency maps (a) 6-phase prototype motor. (b) 6-phase prototype inverter. (c) 6-phase power drivetrain (combined motor & inverter).

D. Validation of enhanced availability of the prototype drivetrain through 3-phase operation

In order to validate enhanced availability in the event of fault on one set of three-phase system of the prototype power drivetrain, it was operated with only A-B-C system supplied by inverter whereas D-E-F system was kept open-circuited. In this operation, both torque and power reduces to half, i.e. the rated torque and the peak torque reduces to 35 N·m and 70 N·m respectively. Fig. 18 compares the predicted and the measured efficiency of the prototype machine with 3-phase operation at the base speed of 2800 r/min. The predicted efficiency in this figure is obtained after calibrating various loss models: (a) iron loss model calibration by 1.24 build factor, (b) copper loss model calibration using measured phase resistance. As seen, measured efficiency matches very well with predicted efficiency except (a) at very low torque (≤ 5 N·m), which may be attributed to accuracy of torque transducer (range 0-200 N·m) at low torque level, and (b) during peak power operation (> 35 N·m), which may be attributed to slightly higher saturation in magnetic circuit in actual prototype machine.

It is worthwhile to note that the copper loss reduces to almost half in 3-phase operation, whereas the iron loss also reduces albeit not to half value, compared to 6-phase operation. Hence, the efficiency of the machine is slightly lower in 3-phase operation compared to 6-phase operation, as the output power also reduces to one half over the entire speed range. The experiment confirms that 50% power is delivered with one 3-phase system in operation albeit with increased torque ripple, vibrations and noise. However, this may not be an adverse issue considering the vehicle has to run only for short duration to reach the safe place for the fault mitigation.

E. Experimental measurement of steady-state short-circuit

As a part of a series of preliminary tests, the steady-state short-circuit current is measured and compared against the FE prediction as shown in Table V. As seen, both matches closely validating FE model used and confirming the machine's capability to tolerate continuous short-circuit current without any overheating as it is only 1% higher than the rated current.

TABLE V

COMPARISON OF MEASURED AND PREDICTED STEADY-STATE SHORT-CIRCUIT CURRENT OF 6-PHASE, 18-SLOT, 8-POLE IPM MACHINE

	Measured	Predicted	% error
SC current at 2800 rpm (peak value)	77.8	79.5	-2.2%

V. DISCUSSION ON FAULT SCENARIOS

The designed machine having the proposed winding configuration with 6-phase, 18-slot, 8-pole exhibits an enhanced availability. In the event of an open-circuit fault in any phase, the 3-phase set with the fault will be disabled and the other 3-phase set will continue to operate with half the torque/power output. In case of a terminal short-circuit in any phase, the other phases will be short-circuited too via the 3-phase inverter with manageable fault current (1.01 times the rated current), and the system continues to operate with the other 3-phase set. The same strategy applies to inter-turn short-circuit upon detection. This enhances the availability of the electric traction power drivetrain without compromising vehicle stability and passenger safety. In this case, the machine will have an unbalanced magnetic pull (UMP) as it will not have the other 3-phase set winding (e.g., D-E-F) to eliminate the unbalanced magnetic pull generated by the healthy 3-phase winding (e.g., A-B-C) in operation. However, this unbalance should not cause any problem in limp-home mode for a maximum battery range. Of course, the faulty part has to be repaired or replaced. The fault tolerant machine characteristics derived from the 6-phase configuration have been validated experimentally and the drive performance under health and one 3-phase open-circuit conditions has also demonstrated. However, the complete functionality of a fault tolerant drive has not been fully tested as this also requires effective fault detection and the tests under laboratory condition need extra hardware for fault emulation. These will be future work.

VI. CONCLUSION

A novel multi-phase permanent magnet machine drive having independent control for both three-phase systems has been designed, analyzed, and tested in healthy (both 3-phase systems in operation) and faulty (only one 3-phase system in operation) modes. The experiments concluded that the drivetrain is able to operate over the torque-speed range and exhibits high efficiency. This drivetrain incorporates redundancy and safety with just one motor, leading to lower footprint, cost saving, and high availability.

ACKNOWLEDGEMENT

The authors gratefully acknowledge the European Commission and CASTOR project partners for permission of the publication of this paper.

REFERENCES

- [1] C. Zwysig, J. W. Kolar, W. Thaler, and M. Vohrer, "Design of a 100 W, 500000 rpm permanent-magnet generator for mesoscale gas turbines," in *IEEE IAS Annu. Meeting. Ind. App. Conf.*, 2005, pp. 253-260 Vol. 1, 2005.
- [2] J. Wang, K. Atallah, Z. Q. Zhu, and D. Howe, "Modular Three-Phase Permanent-Magnet Brushless Machines for In-Wheel Applications," *IEEE Trans. Veh. Tech.*, vol. 57, pp. 2714-2720, 2008.
- [3] L. Sun-Kwon, K. Gyu-Hong, and H. Jin, "Finite Element Computation of Magnetic Vibration Sources in 100 kW Two Fractional-Slot Interior Permanent Magnet Machines for Ship," *IEEE Trans. Mag.*, vol. 48, pp. 867-870, 2012.
- [4] E. M. Tsampouris, M. E. Beniakar, and A. G. Kladas, "Geometry Optimization of PMSMs Comparing Full and Fractional Pitch Winding Configurations for Aerospace Actuation Applications," *IEEE Trans. Mag.*, vol. 48, pp. 943-946, 2012.
- [5] C. Yicheng, P. Pillay, and A. Khan, "PM wind generator topologies," *IEEE Trans. Ind. Applicat.*, vol. 41, pp. 1619-1626, 2005.
- [6] J. Wang, X. Z. Ping, and D. Howe, "Three-phase modular permanent magnet brushless Machine for torque boosting on a downsized ICE vehicle," *IEEE Trans. Veh. Tech.*, vol. 54, pp. 809-816, 2005.
- [7] K. Atallah, W. Jiabin, and D. Howe, "Torque-ripple minimization in modular permanent-magnet brushless machines," *IEEE Trans. Ind. Applicat.*, vol. 39, pp. 1689-1695, 2003.
- [8] C. Shi-Uk, K. Jong-Moo, K. Dae-Hyun, W. Byung-Chul, H. Do-Kwan, and L. Ji-Young, "Fractional Slot Concentrated Winding Permanent Magnet Synchronous Machine With Consequent Pole Rotor for Low Speed Direct Drive," *IEEE Trans. Mag.*, vol. 48, pp. 2965-2968, 2012.
- [9] T. T. Oikawa, K. Masumoto, H. Akita, H. Kawaguchi, and H. Kometani, "Development of high efficiency brushless DC motor with new manufacturing method of stator for compressors," *Inter. Compressor Engg. Conf.*, 2002.
- [10] A. G. Jack, B. C. Mecrow, P. G. Dickinson, D. Stephenson, J. S. Burdess, N. Fawcett, and J. T. Evans, "Permanent-magnet machines with powdered iron cores and prepressed windings," *IEEE Trans. Ind. Applicat.*, vol. 36, pp. 1077-1084, 2000.
- [11] Z. Q. Zhu and D. Howe, "Influence of design parameters on cogging torque in permanent magnet machines," *IEEE Trans. Ener. Conv.*, vol. 15, pp. 407-412, 2000.
- [12] N. Bianchi, S. Bolognani, M. D. Pr e, and G. Grezzani, "Design considerations for fractional-slot winding configurations of synchronous machines," *IEEE Trans. Ind. Applicat.*, vol. 42, pp. 997-1006, 2006.
- [13] Z. Q. Zhu, D. Ishak, D. Howe, and C. Jintao, "Unbalanced Magnetic Forces in Permanent-Magnet Brushless Machines With Diametrically Asymmetric Phase Windings," *IEEE Trans. Ind. Applicat.*, vol. 43, pp. 1544-1553, 2007.
- [14] J. K. Tangudu, T. M. Jahns, and A. El-Refaei, "Unsaturated and saturated saliency trends in fractional-slot concentrated-winding interior permanent magnet machines," in *IEEE Ener. Conv. Cong. and Expo. (ECCE)*, pp. 1082-1089, 2010.
- [15] J. D. Ede, K. Atallah, G. W. Jewell, J. B. Wang, and D. Howe, "Effect of Axial Segmentation of Permanent Magnets on Rotor Loss in Modular Permanent-Magnet Brushless Machines," *IEEE Trans. Ind. Applicat.*, vol. 43, pp. 1207-1213, 2007.
- [16] G. Dajaku, "Elektrische Maschine," *DE 102008 057 349 B3*, July 15, 2010.
- [17] P. B. Reddy, H. Kum-Kang, and A. M. El-Refaei, "Generalized Approach of Stator Shifting in Interior Permanent-Magnet Machines Equipped With Fractional-Slot Concentrated Windings," *IEEE Trans. Ind. Electron.*, vol. 61, pp. 5035-5046, 2014.
- [18] J. Wang, V. I. Patel, and W. Wang, "Fractional-Slot Permanent Magnet Brushless Machines with Low Space Harmonic Contents," *IEEE Trans. Mag.*, vol. 50, pp. 1-9, 2014.
- [19] E. Levi, "Multiphase Electric Machines for Variable-Speed Applications," *IEEE Trans. Ind. Electron.*, vol. 55, pp. 1893-1909, 2008.
- [20] M. Villani, M. Tursini, G. Fabri, and L. Castellini, "High Reliability Permanent Magnet Brushless Motor Drive for Aircraft Application," *IEEE Trans. Ind. Electron.*, vol. 59, pp. 2073-2081, 2012.
- [21] S. Sadeghi, G. Lusu, H. A. Toliyat, and L. Parsa, "Wide Operational Speed Range of Five-Phase Permanent Magnet Machines by Using Different Stator Winding Configurations," *IEEE Trans. Ind. Electron.*, vol. 59, pp. 2621-2631, 2012.
- [22] L. De Lillo, L. Empringham, P. W. Wheeler, S. Khwan-On, C. Gerada, M. N. Othman, and H. Xiaoyan, "Multiphase Power Converter Drive for Fault-Tolerant Machine Development in Aerospace Applications," *IEEE Trans. Ind. Electron.*, vol. 57, pp. 575-583, 2010.
- [23] M. O. E. Aboelhassan, T. Raminosa, A. Goodman, L. de Lillo, and C. Gerada, "Performance Evaluation of a Vector-Control Fault-Tolerant Flux-Switching Motor Drive," *IEEE Trans. Ind. Electron.*, vol. 60, pp. 2997-3006, 2013.
- [24] M. T. Abolhassani and H. A. Toliyat, "Fault tolerant permanent magnet motor drives for electric vehicles," in *IEEE Inter. Elect. Mach. Drives Conf. (IEMDC)*, pp. 1146-1152, 2009.

- [25] C. J. Ifedi, B. C. Mecrow, S. T. M. Brockway, G. S. Boast, G. J. Atkinson, and D. Kostic-Perovic, "Fault-Tolerant In-Wheel Motor Topologies for High-Performance Electric Vehicles," *IEEE Trans. Ind. Appl.*, vol. 49, pp. 1249-1257, 2013.
- [26] D. Yazdani, S. A. Khajehoddin, A. Bakhshai, and G. Joos, "Full Utilization of the Inverter in Split-Phase Drives by Means of a Dual Three-Phase Space Vector Classification Algorithm," *IEEE Trans. Ind. Electron.*, vol. 56, pp. 120-129, 2009.
- [27] H. Jin, L. Bingnan, J. Haibo, and K. Min, "Analysis and Control of Multiphase Permanent-Magnet Bearingless Motor With a Single Set of Half-Coiled Winding," *IEEE Trans. Ind. Electron.*, vol. 61, pp. 3137-3145, 2014.
- [28] N. Bodo, M. Jones, and E. Levi, "A Space Vector PWM With Common-Mode Voltage Elimination for Open-End Winding Five-Phase Drives With a Single DC Supply," *IEEE Trans. Ind. Electron.*, vol. 61, pp. 2197-2207, 2014.
- [29] R. Kianinezhad, B. Nahid-Mobarakeh, L. Baghli, F. Betin, and G. A. Capolino, "Modeling and Control of Six-Phase Symmetrical Induction Machine Under Fault Condition Due to Open Phases," *IEEE Trans. Ind. Electron.*, vol. 55, pp. 1966-1977, 2008.
- [30] F. Immovilli, C. Bianchini, E. Lorenzani, A. Bellini, and E. Fornasiero, "Evaluation of Combined Reference Frame Transformation for Inter-turn Fault Detection in Permanent Magnet Multi-Phase Machines," *IEEE Trans. Ind. Electron.*, vol. PP, pp. 1-1, 2014.
- [31] V. Patel, J. Wang, J. Touse, X. Motger, T. Hoffmann, R. Vuletic, . . . R. Bahr, "Subsystems specification report," FP7 - CASTOR Project Deliverable D1.4, 2011.
- [32] P. Morrison, A. Binder, B. Funieru, and C. Sabirin, "Drive train design for medium-sized zero emission electric vehicles," in 13th European Conf. Power Electr. and Appl., 2009. EPE '09., pp. 1-10, 2009.
- [33] V. I. Patel, J. Wang, W. Wang, and X. Chen, "Analysis and design of 6-phase fractional slot per pole per phase permanent magnet machines with low space harmonics," in *IEEE Inter. Elect. Mach. Drives Conf. (IEMDC)*, pp. 386-393, 2013.
- [34] J. Wang, X. Yuan, and K. Atallah, "Design Optimization of a Surface-Mounted Permanent-Magnet Motor With Concentrated Windings for Electric Vehicle Applications," *IEEE Trans. Veh. Tech.*, vol. 62, pp. 1053-1064, 2013.
- [35] V. I. Patel, J. Wang, W. Wang, and X. Chen, "Thermal design and analysis of 6-phase fractional slot permanent magnet machines considering driving cycles," in 7th IET Inter. Conf. Power Electr., Mach. Drives (PEMD 2014), pp. 1-6, 2014.
- [36] P. Lazari, J. Wang, and L. Chen, "A computationally efficient design technique for electric vehicle traction machines," in XXth Inter. Conf. Electr. Mach. (ICEM), 2012, pp. 2596-2602, 2012.
- [37] T. Jalakas, D. Vinnikov, and J. Laugis, "Evaluation of different loss calculation methods for high-voltage IGBT-s under small load conditions," in *Power Electr. Motion Control Conf.*, 2008. EPE-PEMC 2008. 13th, pp. 1263-1267, 2008.
- [38] H. Yashan, Z. Zi-Qiang, and L. Kan, "Current Control for Dual Three-Phase Permanent Magnet Synchronous Motors Accounting for Current Unbalance and Harmonics," *IEEE Journal of Emerg. Select. Topics Power Electr.*, vol. 2, pp. 272-284, 2014.



Vipulkumar I. Patel (M'13) received the B.E. degree in electrical engineering from Nirma Institute of Technology, Gujarat University, Ahmedabad, India, in 2003, the M.Tech. degree in power electronics, electrical machines, and drives from the Indian Institute of Technology Delhi, New Delhi, India, in 2005, and Ph.D. degree in electronic and electrical engineering from The University of Sheffield, Sheffield, U.K., in 2014.

He is currently a Research Assistant in electronic and electrical engineering with The University of Sheffield. From 2005 to 2010, he was a Lead Engineer with the GE India Technology Centre, Bangalore, India. His research interests include design and analysis of permanent-magnet machines for electric traction applications.

Dr. Patel was a recipient of the IEEE Power Electronics, Drives and Energy Systems '96 Award for the Best Performance in the Area of Power Electronics, Electrical Machines & Drives in 2005.



Jiabin Wang (SM'03) received the B.Eng. and M.Eng. degrees from Jiangsu University of Science and Technology, Zhengjiang, China, in 1982 and 1986, respectively, and the Ph.D. degree from the University of East London, London, U.K., in 1996, all in electrical and electronic engineering.

Currently, he is a Professor in Electrical Engineering at the University of Sheffield, Sheffield, U.K. From 1986 to 1991, he was with the Department of Electrical Engineering at Jiangsu University of Science and Technology, where he was appointed a Lecturer in 1987 and an Associated Professor in 1990. He was a Postdoctoral Research Associate at the University of Sheffield, Sheffield, U.K., from 1996 to 1997, and a Senior Lecturer at the University of East London from 1998 to 2001. His research interests range from motion control and electromechanical energy conversion to electric drives for applications in automotive, renewable energy, household appliances and aerospace sectors.

He is a fellow of the IET and a senior member of IEEE.



Dian Tresna Nugraha received the Sarjana Teknik (B.Eng.) of Electronic Engineering in Institut Teknologi Bandung, Indonesia and M.Sc. degree in Communication Engineering from Universität Karlsruhe (TH), Germany, in 2001 and 2003, respectively.

After completing the study, he continued working at Infineon Technologies A.G. in the Motorsport Electronic department supplying Electronic Control Unit for Formula 1 Racing team. He is currently a Senior Staff Engineer Automotive System Engineering at Infineon Technologies A.G. and has been working since 2008 on the topics of controllers and algorithms for electric motor drive, power converters, and safety-related automotive systems.



Radovan Vuletić received the Diploma degree (M.Sc.) in electrical engineering from the University of Novi Sad, Serbia, in 1996.

From 1996 to 2000, he was with Sever Electrical Machines A.D., Subotica, Serbia as Senior Industrial Controls Engineer. From 2000 to 2009, he was with Infineon Technologies AG/Qimonda AG, Munich, Germany as a Staff Product Development Engineer.

From October 2010, he continued working for the Infineon Technologies AG as a Senior Staff System Engineer responsible for concept, simulation and HW design of electrical automotive systems. His research interests include systems in the hybrid- and electric vehicles, electrical motor drives, DC/DC converters and on-board chargers.



Jonas Touse holds a diploma (Dipl.-Ing.) in mechanical engineering with focus on mechatronics from the Technical University of Braunschweig, Germany.

After completing his studies in 2008, he continued working at Volkswagen, where he had been active already during his studies and his thesis. He started off as a project leader for several Plug-In Hybrid Electric Vehicles (PHEV) projects in the powertrain department. Since 2012, he is responsible for the development of e-motors for Battery Electric Vehicles (BEV) and Fuel Cell Electric Vehicles (FCEV).